https://doi.org/10.5194/egusphere-2022-416
Preprint. Discussion started: 8 July 2022

This is very nice paper, giving a complete overview of a spectroscopic data reduction chain, including link to a significant data set.

Spectral Observations at the CILBO Observatory: Calibration and Data Sets

Joe Zender[1], Detlef Koschny[1,6], Regina Rudawska[2], Salvatore Vicinanza[3], Stefan Loehle[4], Martin Eberhart[4], Arne Meindl[4], Hans Smit[1], Lionel Marraffa[1], Rico Landman[5], and Daphne Stam[3]

[1]European Space Research and Technology Centre (ESA ESTEC), 2200 AG Noordwijk, The Netherlands
[2]RHEA group/ESA ESTEC, 2200 AG Noordwijk, The Netherlands
[3]Faculty of Aerospace Engineering, Delft University of Technology, Delft, The Netherlands
[4]IRS, University of Stuttgart, Germany
[5]Leiden Observatory, Leiden University, Postbus 9513, 2300 RA, Leiden, The Netherlands
[6]Chair of Astronautics, TU Munich, 85748 Garching, Germany

Correspondence: Joe Zender (Joe.Zender@esa.int)

Abstract. The Canary Island Long-Baseline Observatory (CILBO) is a double station meteor camera setup located on the Canary Islands and operated by ESA's Meteor Research Group since 2010. Observations of meteors are obtained in the visual wavelength band by intensified video cameras from both stations, supplemented by an intensified video camera mounted with a spectral grating at one of the locations. The cameras observe during cloudless and precipitation-free nights and data are transferred to a main computer located at ESA/ESTEC once a day. The image frames that contain spectral information are calibrated, corrected, and finally processed into line intensity profiles. An ablation simulation, based on Bayesian statistics using a Markov-Chain Monte-Carlo method, allows to determine a parameter space, including the ablation temperatures, chemical elements and their corresponding line intensities, to fit against the line intensity profiles of the observed meteor spectra. The algorithm is presented in this paper and one example is discussed. Several hundred spectra have been processed and made available through the Guest Archive Facility of the Planetary Science Archive of ESA. The data format and meta-data are explained.

1 Introduction

Main insights in the dust composition of our solar system have been obtained during the past decade. Ground-based observations from ultraviolet to radio wavelengths (Snodgrass et al., 2017), space-based telescopes, such as HST (Hadamcik et al., 2016), direct space-based remote-sensing and in-situ observations as obtained by the Rosetta spacecraft during its two year nominal mission lifetime (Rubin et al., 2020; Rivilla et al., 2020; Altwegg et al., 2020), and laboratory analysis of samples returned back to Earth, e.g. by the STARDUST mission (Brownlee, 2014), have provided valuable datasets. A summary of our current knowledge of cometary dust is given in Levasseur-Regourd et al. (2018). For interplanetary dust in general, see Koschny et al. (2019) and references therin. The knowledge of dust allows us to derive further information on e.g. the origin and further evolution of comets (Rubin et al., 2020). Another, indirect way to observe dust is the observation of meteors, thus the observation of the ablation process of meteoroids through Earth's atmosphere. To allow the chemical analysis of the abla-

https://doi.org/10.5194/egusphere-2022-416
Preprint. Discussion started: 8 July 2022

tion process, spectral observations are needed and have been successfully demonstrated by several teams in the past decades (Vojáček et al., 2019; Borovička et al., 2005; Abe et al., 2020; Ward, 2017; Madiedo, 2015; Jenniskens et al., 2014; Rudawska et al., 2014; Zender et al., 2002; Matlovič et al., 2019; Vojáček et al., 2019; Zender, 1994).

ESA's Meteor Research Group (MRG) maintains a number of cameras acquiring the meteor ablation phenomena in Earth's atmosphere, also known as shooting stars or fireballs for brighter events. A general overview of our activities is given in Koschny et al. (2015a).

Besides supporting campaign-based observations (Koschny et al., 2012; Vaubaillon et al., 2015), the MRG maintains a permanent, double station on the Canary Islands acquiring videos from two distinct locations. The parallel acquisition of meteors allows to derive geometric information through trigonometric algorithms (Koschny et al., 2013a). In one of the CILBO stations, a dedicated camera is equipped with a spectral grating to acquire spectral information of the brightest meteors throughout the ablation process in the Earth atmosphere (Zender et al., 2014).

In this paper, we describe the data reduction process from the acquired images to the final spectra.

A full algorithm to derive meteor spectra was discussed in the middle of the twentieth century by Ceplecha (1971). His observations were executed at the Ondřojev Observatory and based on the usage of photographic cameras acquiring a long-exposure in the visual wavelength regime. Spectral plates or spectral prisms diffracted the lights source, e.g. light from a star or from a meteor, into its spectral components. Once the photographic plate was developed, the light curve was measured using a device named micro-densitometer, e.g. the Mann 1140 or the Lirepho2 [1] micro-densitometer. The wavelength identification along the obtained light curve was directly computed due to the availability of the zero-order of the meteor using an earlier algorithm of Ceplecha (1961). Given an in-falling vector (the zero-order of the meteor) on the grating plate, the algorithm computes the (x,y)-position for each wavelength on the focal plane, taking into account rotations between the grating plate reference frame and the optical axes.

Quantitative analysis of meteor spectra was introduced by several observers (Borovicka, 1994a, b; Jenniskens, 2007). The observations and analysis of Borovicka (1994a) identified two main thermal components during the ablation process, a low-temperature component of about 4000 K and a hot-component of 10000 K. Jenniskens (2007) provides a summary of all identified elements and confirms the two thermal components, complemented by the formalism to derive the number densities for chemical elements. The calibration of the wavelength scale is achieved by laboratory measurements using a Mercury-Argon calibration source applied over different source incidence angles. These allow at a later step in the algorithm to confirm the correct distances between potential line intensities of different elements. The wavelength scale is described as nearly linear, which overcomes the problem of the diffraction hyperbola that is the effect of a curved spectrum due to a non-optimal * lens. The projection of a meteor spectrum onto an image is only linear under the assumption of an optimal lens (Ceplecha, 1961). The projection of an optimal lens onto an imaging plane, i.e. CCD detector, is gnomonic. In video systems used in the last three decades this is however not given and Dubs and Schlatter (2015) proposes an additional image transformation to transform an acquired image into an gnomonic projection.

I do not immediately how, but will look up in Borovicka paper.

-> propose?

[1] Lirepho is an acronym for "lichtelektrisches Registrierphotometer" produced by Zeiss

* I got at first slightly confused with what is meant with the wording 'non-optimal' lens: is it a lens that suffer from imperfections (aberrations)?, or is it a lens that has a projection formula that does not match the preferred one? From the explanation I clearly understand that the latter is meant and that the optimal lens for this work is a lens with a gnomonic projection. These lenses indeed are rare. Nonetheless I would suggest to replace 'a non-optimal lens' with 'the lens'. Then the rest of the section is self explanatory I believe.

https://doi.org/10.5194/egusphere-2022-416
Preprint. Discussion started: 8 July 2022

This paper presents the CILBO observation locations and hardware (Chapter 2) and the data processing steps applied to the meteor spectra: the individual video frames are radiometricaly processed (Chapter 3) and converted into the FITS format. In case the visual camera has observed the zero-order and the grating camera has observed the first-order spectrum of the meteor, the wavelengths are computed for each individual frame (Chapter 4) and we obtain a spectral profile. In the following, an intensity correction is applied to the spectral profile (Chapter 6). To determine the temperature regime and the chemical elements that optimally match the obtained spectral profile, we simulate the spectral response of several elements at different temperatures and use these simulated values applying the Bayesian methodology (Chapter 7) combined with a Markov-Chain Monte Carlo (MCMC) sampling. As a result we obtain the line intensities which are then further corrected to the corresponding number densities of the elements by integrating the column densities over the line of sight (Chapter 6).

-> 'imaging' instead of 'visual'

The data pipeline is then briefly discussed (Chapter 8) using one meteor spectrum. In Chapter 9 we describe the datasets that we make available as supplement to this paper.

2 The Canary Island Long-baseline Observatory: CILBO

2.1 Equipment

The Meteor Research Group (MRG) of the European Space Agency operates the double-station meteor camera system CILBO (Canary Island Long-Baseline Observatory)(Koschny et al., 2014). Several image-intensified video cameras are operated on Tenerife at the Izaña Observatory, and on La Palma at the Observatorio del Roque de los Muchachos. A photograph of one of the cameras is shown in Figure 1. Table 2.1 provides details on the individual cameras and locations.

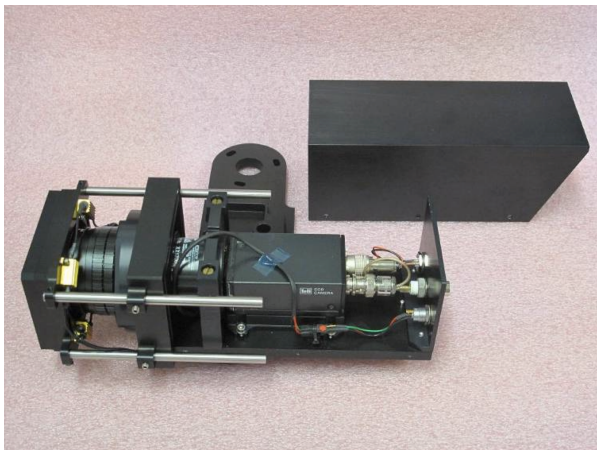

Figure 1. Photograph of one of the intensified video cameras equipped with a grating. The protective cover is removed and visible in the back. Power resistors to heat the grating can be seen on the left

https://doi.org/10.5194/egusphere-2022-416
Preprint. Discussion started: 8 July 2022

I miss Table caption

Tenerife (28.3011°N, -16.5119°W, 2395m)			
Camera Name	Detector	Optics	Spectral Grating
ICC7	Fujinon CF-25L	25 mm, f/0.85	
ICC8	Fujinon CF-25L	25 mm, f/0.85	Zeiss, 611 grooves/mm
La Palma (28.7600°N, -17.8824°W, 2327m)			
Camera Name	Detector	Optics	Spectral Grating
ICC9	Fujinon CF-25L	25 mm, f/0.85	

The cameras ICC7 and ICC9 acquire videos with their line-of-sights pointing to a point 100 km above the Earth's surface, at a location between the two islands, at 28.5533°N and -17.1667°W. The so-called spectral camera ICC8 is offset to ICC7 by 23.0° to capture the first order spectrum of meteors passing through the field of view of camera ICC7. A technical overview drawing is shown in Figure 2.

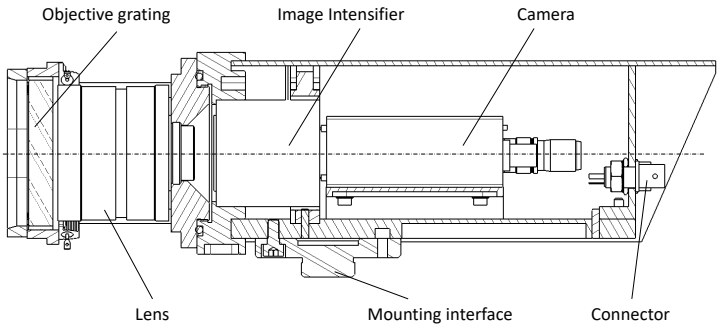

Figure 2. Technical drawing of one of the intensified video cameras.

The camera systems use a low-distortion machine-vision lense from Fujinon, imaging the sky onto the entrance aperture of a second-generation image intensifier (DEP XX-1700). The intensifier has a spectral sensitivity from about 350 to 850 nm. It is fibre-coupled to a charge-coupled device (CCD), which is read out via a Toshiba Teli CS8310Bi PAL video camera. The PAL format has 576×768 pixel^2. Full frames are read out per second with 8 bit dynamical accuracy. With the given field of view the pixel scale is $2.3'$. A dew remover (type Kendrick) is wrapped around the objective lens to avoid dewing.

https://doi.org/10.5194/egusphere-2022-416
Preprint. Discussion started: 8 July 2022

Table 1. Meteor events acquired from ICC7 and ICC8 systems since year 2012. Columns *ICC7 Events* and *ICC8 Events* give the number of events recorded by ICC7 and ICC8, respectively. Column *Simultaneous Events* gives the number of events recorded simultaneously by both ICC7 and ICC8. The last row gives the total number of events recorded since 2012.

Year	*ICC7 Events*	*ICC8 Events*	*Simultaneous Events*	*ICC9 Spectral Events*
2012	11312	19492	4127	91
2013	19435	10385	667	110
2014	12647	4884	195	39
2015	18377	25423	5286	54
2016	27481	24135	2734	48
2017	10388	9050	684	12
2018	1150	484	147	1
2019	3088	1262	335	0
2020	0	1077	0	0
Total	103622	96231	14174	355

I think ICC8 is the spectral camera, isn't it? Probably you want to state that this column shows all ICC9 hits that also have a spectrum on ICC8. (But I'm not sure, as I would not expect that ICC8 has so many spectra. Are ICC8 and IC9 maybe interchanged?).

Assuming that the last column is the spectral camera, is the fact that you capture in 2012/13 the most spectra, but not the max number of meteors in the two imaging camera's, already to be associated with degradation of the grating?

2.2 Control Software

The core of the software is the detection software MetRec (Molau, 1999, find reference) that analyses the image streams from ICC7 and ICC9, independently from each other. The ICC8 camera image stream is read into a separate detection software called SpecRec on the computer of ICC7. In case the MetRec detection software of camera ICC7 detects a meteor, a hardwired trigger signal (RS232 serial port) is transferred to the ICC8 detection software. The image stream including the three images acquired before the trigger signal arrived are stored onto a hard disk. The MetRec software stores for each individual frame of each detected meteor event the right ascension and declination of the photometric centre of the meteor and the magnitude. It also stores an estimate of the cloud coverage with one minute accuracy. The computers are synchronised to a network-provided time signal every two minutes. A more detailed description of CILBO setup and its cameras is available in Koschny et al. (2013b).

2.3 System Performance

Since its start of operations in 2012, the cameras ICC7 and ICC8 have individually recorded over 90 000 meteor events, as indicated in Table 1. To apply the wavelength calibration on these events, the calibration routine we have developed requires that both zero-order images recorded by ICC7 and first-order spectra from ICC8 be available simultaneously (further explained in Section 4). About 14 000 were recorded by both systems simultaneously. The distribution of these events per year is listed in the column *Simultaneous Events* of Table 1.

See Koschny et al. (2017) for a more detailed analysis covering 2012 to 2017. The 3D trajectory and heliocentric orbits of these meteoroids were computed using the MOTS (Meteor Orbit and Trajectory Software) code (Koschny and Diaz del Rio,

https://doi.org/10.5194/egusphere-2022-416
Preprint. Discussion started: 8 July 2022

2002; Koschny et al., 2015b). Column *ICC9 Spectral Events* in Table 1 refer to the identified, full spectra obtained. In this paper, we focus on the analysis from 2012 to 2017, as afterwards the tranmissivity of the grating has been degraded. We have also excluded spectra that are not fully contained in all frames of the meteor event.

3 Radiometric Correction and Background Subtraction

Each detected meteor event results in a number of bitmap (BMP) images files for ICC7 and ICC8, as well as an "information file" for ICC7 which contains measurement results for the meteor. The image files contain the three images acquired before the first detection of the event, as well as three images after the meteor event is lost.

As the CILBO setup has not foreseen a camera door or shutter, a dark current image is only available from the time of the initial setup of the overall system in 2012. A flatfield image is produced synthetically taking the median values for each pixel of an image sequence obtained on a clear night, and then used throughout the years. First, all images, including the pre- and post-images, are radiometrically corrected by dark current subtraction and the flat-field division.

are you this way seriously affected by hot pixels, etc.?

I understand you change update the flatfield periodically.

To compensate for acquisitions taken during cloudy conditions or during dawn or dusk, the six radiometrically processed pre-event and post-event images are stacked together into a background image: for each pixel, the median value of the six available pixel is taken.

Each radiometrically processed image in the meteor sequence is then subtracted by this background image. This operation also subtracts the stars from the images and would result in a low background image in case no spectrum is visible. A so-called total image is created by selecting for each pixel location the median pixel value of all images of the meteor sequence obtained so far. The total image provides a summary of the full meteor event and allows to have a quick look on an event and judge the spectrum brightness.

median value chosen to avoid saturation (contrary to max value)?

The obtained image sequence as well as the total image, dark current and flatfield, are stored in a single FITS-formatted file, referenced as *level-0 dataset* (see Chapter 9 for a detailed description).

4 Wavelength Determination

Different to other algorithms described so far (Borovicka, 1994a; Dubs and Schlatter, 2015), our algorithm determines the pixel position as a function of wavelength in the ICC8 image, computed from the position in the zero-order image from ICC7. This is done by taking the angular offset between the two cameras into account. The basic idea of this step can be best compared to the 2-dimensional diffraction formulae as we know it from the single-slit optical diffraction experiment:

is this offset calibrated periodically? or is the mount that stable?

$$\sin\theta = \lambda/d \tag{1}$$

Knowing the wavelength λ and the slit width d, one can compute the angle θ and thus the location of the maxima and minima.

https://doi.org/10.5194/egusphere-2022-416
Preprint. Discussion started: 8 July 2022

Assuming a Fraunhofer's diffraction at the grating, the light of a star or meteor is considered as parallel entering light rays and its resulting diffraction can be expressed using the 3-dimenional grating formulae as provided in equation (2).

$$\overrightarrow{v^{Lens}}(\lambda) = \begin{pmatrix} -x^{Grating} - (n\lambda d) \\ -y^{Grating} \\ \sqrt{(1 - \left(x^{Grating} + (n\lambda d)\right)^2 - (y^{Grating})^2)} \end{pmatrix} \quad (2)$$

best explain also what v_Lens means

with:

- $(x,y)^{Grating}$ are the coordinates on the grating, at which the light enters
  -> on and in the plane of the grating
- n is the grating order which has +1 as nominal value;
- λ is the wavelength (in meter);
- d is the groove density (in number of grooves per meter).

With the information from ICC9, especially the right ascension and declination of the meteor, the zero-order, for each individual frame, the diffraction vector $d(\lambda)$ for any wavelength λ can be calculated. To derive the (x,y) coordinates at the CCD frame, a sequence of reference frame transformations has to be applied. We further assume that all reference frames are right-handed ones and that the reference frames' z-axes are aligned to each other, in particular the CCD, the optical, and the grating z-axes.

please explain (with a picture?)

As a first step, we have to derive the $(x,y)^{Grating}$ coordinates of equation 2, by applying the following reference frame transformations:

- $\mathcal{F}_{Celestial} \longrightarrow \mathcal{F}_{LocalHorizon}$
  This transformation converts a meteor position (right ascension and declination in J2000, as obtained from ICC9 information) for a given time from the Earth centred celestial frame into an observer centred frame (altitude, hour angle), with the horizon as the fundamental frame. [2]

- $\mathcal{F}_{LocalHorizon} \longrightarrow \mathcal{F}_{Grating}$
  This transformation converts a meteor position (altitude and hour angle) for a given time from the observer based frame into a grating centered reference frame. This conversion requires the knowledge of the azimuth and elevation of the +x–axis and +y–axis of the grating, respectively. Assuming that it is identical to the optical axis of the complete camera system, it can be computed from the right ascension and declination of the center of the field of view at any given time. The boresight angle allows for a non-horizontal plate. Unfortunately, this value was not measured at the time of the CILBO installation and we use a rotation value of -11.0 degree as best fit value in the z–axis. The tilt angle describes a rotation of the grating, a rotation of the x–y–plane of $\mathcal{F}_{Grating}$ perpendicular to the +z axis of the grating. If these angles

this is the angle that the z-axis of the grating is tilted?

[2] The python routine *eq2hor* is used.

https://doi.org/10.5194/egusphere-2022-416
Preprint. Discussion started: 8 July 2022

are known, a transformation matrix can be constructed to convert any vector in the horizontal frame into a vector in the grating frame as follows:

$$\boldsymbol{x}^{Grating} = M_{azimuth} \cdot M_{elevation} \cdot M_{boresight} \cdot M_{tilt} \cdot \boldsymbol{x}^{LocalHorizon} \tag{3}$$

– $\mathcal{F}_{Grating} \longrightarrow \mathcal{F}^{\lambda}_{Lens}$ can be determined with equation 2, and produces for each wavelength λ a vector.
From the vector $\overrightarrow{v^{Lens}(\lambda)}$ one could directly transform into the CCD frame and obtain the (x,y) coordinates of the image by normalizing the z–component of $\overrightarrow{v^{Lens}(\lambda)}$ to 1. From the known field-of-view of the camera, one can construct vectors from the CCD center to the field-of-view corners assuming again that the z-component equals to 1. From these relations we can derive the x-position and y-position of the meteor directly. in de CCD frame is it not better to state that this follows from the focal length and pixelsize?

We follow a different approach, and transform the obtained vectors back in an inverse transformation into $\mathcal{F}^{\lambda}_{Celestial}$ by applying the inverse matrices of equations 2 and 3. As a result, we obtain the Celestial coordinates for each wavelength. With the knowledge of the plate constant of the camera, these coordinates can be directly transformed into the image (x,y) coordinates. [3] To allow this last transformation, we use the web-service offered by astrometry.net (Lang et al., 2010)[4] to obtain a registered image. This registration was done once with an image under good seeing conditions. As the web-service registration also takes the geometric distortions into account, the algorithm does not need to apply any additional distortion correction routines.

The calibration step results for each frame in a list of wavelengths and its corresponding digital value at the computed image position and is stored in a single FITS file labeled as *level-1 dataset* (see section 9 for a detailed description).

It is noted that the accuracy of our algorithm - determined through the correct identification of the (x,y) position of a maxima for a chemical element - was not always satisfactory. As the bright pixels representing the zero-order meteor in ICC9 are spread over many pixels, a centroid algorithm is used in METREC, that did not always correspond to the centre pixel of the meteor as visually observed. The difference was within a few pixels, however the impact on the overall accuracy of the algorithm was too large to neglect. The problem was corrected in a later processing step (see Section 7.2) by adding the wavelength itself as one of the Bayesian parameters.

5 Spectral Calibration

5.1 Spectral Response of ICC8

The spectral response curve for ICC8 was derived from images containing the first order spectrum of Vega.

Vega is an A0-type star with a well-known emission spectrum in the visible range. A reference spectrum of Vega was taken from STIS[5]. To obtain an ICC8 Vega spectrum, four frames acquired on four consecutive days were selected. Each frame is

[3] Using the python routine xxxx.
[4] http://nova.astrometry.net
[5] CALSPEC Archive: https://archive.stsci.edu/hlsps/reference-atlases/cdbs/current_calspec/

https://doi.org/10.5194/egusphere-2022-416
Preprint. Discussion started: 8 July 2022

then radiometrically processed and the wavelength are derived as provided in section 3 and 4. The final observed Vega spectrum is the median of the four calibrated and atmospheric-corrected spectra. ICC8 spectral response curve is the ratio between the final observed spectrum and the reference spectrum, fitted with a 12-th order polynomial, and normalized to 1, as shown in Figure 3. To validate the ICC8 spectral response, acquired spectra of Algol, Castor, Deneb, Elnath, and Vega underwent our calibration pipeline and were compared to the spectra provided in CALSPEC or HyperLeda[6]

It would be interesting to report on the outcome or include a picture with the results.

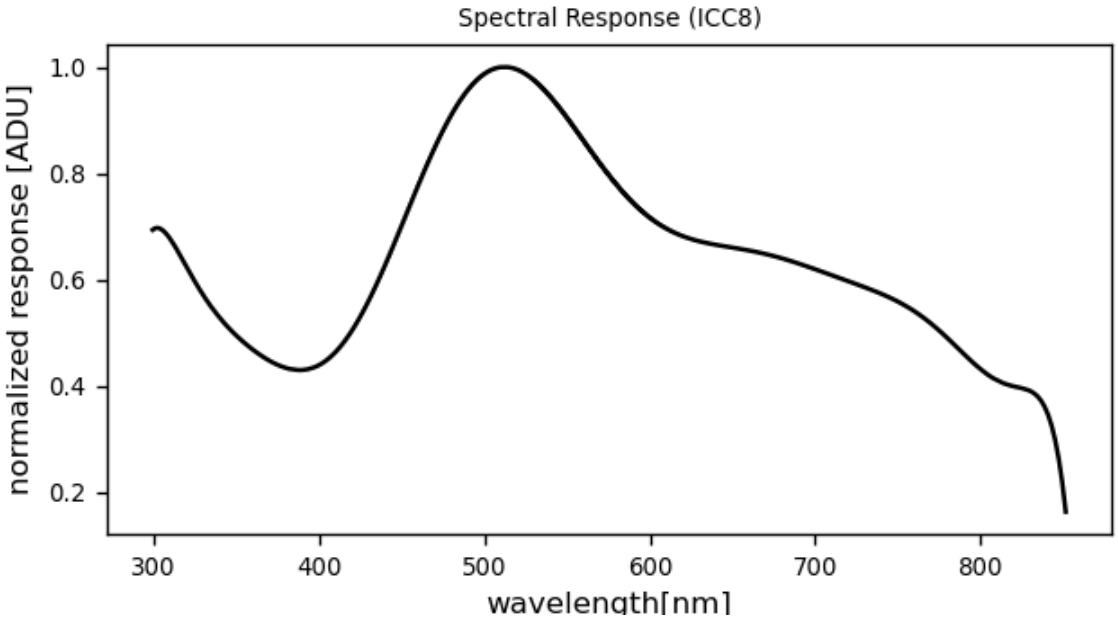

Figure 3. Normalized ICC8 spectral response curve

5.2 Correction of Atmospheric Attenuation

As the light emitted from the ablation process undergoes atmospheric extinction, we apply a correction to the spectral response curves as obtained in Section 5. The scattering and absorption correction is applied to each individual frame and depends on the exact observation geometry, especially the Zenith angle of the observed meteor θ_{met} and the optical thickness b_{met} of the atmosphere. The extinction law can be described as a correction vector (Appenzeller, 2013), as follows:

$$\overrightarrow{v_{corr}} = \frac{\overrightarrow{F_{0,met}}}{\overrightarrow{F_{met}}} = \frac{1}{\exp\left(\frac{\overrightarrow{-b_{met}}}{\cos(\theta_{met})}\right)} \tag{4}$$

[6]HyperLeda[2]: http://leda.univ-lyon1.fr/

https://doi.org/10.5194/egusphere-2022-416
Preprint. Discussion started: 8 July 2022

where $\overrightarrow{F_{met}}$ represents the intensity of each feature of the observed meteor spectrum, and $\overrightarrow{F_{0,met}}$ the intensities of the true, atmospheric-corrected, spectrum. The atmospheric optical thickness is a coefficient specifying the attenuation of light through the atmosphere; $\overrightarrow{b_{met}}$ is a vector varying with wavelength. In case we consider only scattering contributing to the atmospheric extinction, $\overrightarrow{b_{met}} = \overrightarrow{b_{sca}}$ is obtained as in Equation (5), with N_{gas} the column number density of gas molecules (obtained using Equation 6) and σ_{sca} the scattering cross section of gas molecules (obtained with Equation (7)).

$$\overrightarrow{b_{met}} = \overrightarrow{b_{sca}} = N_{gas} \cdot \sigma_{sca} \tag{5}$$

In note that the effect of Aerosols is not considered (as described in Vicinanza 2021. What is the reason for this?

$$N_{gas} = \frac{p_{bottom} - p_{top}}{m_{gas} \cdot g} \tag{6}$$

$$\sigma_{sca}(\lambda) = \frac{24\pi^3}{N_L^2} \frac{(n^2-1)^2}{(n^2+2)^2} \frac{(6+3\delta)}{(6-7\delta)} \frac{1}{\lambda^4} \approx \frac{C}{\lambda^4} \tag{7}$$

m_{gas} is the air mass (obtained for dry air conditions (28.96 g/mol)) and g the gravitational acceleration (9.806 m/s^2), both considered constant through the atmosphere. p_{bottom} and p_{top} are the pressures at the altitudes of the atmosphere corresponding to the begin and end of the meteor ablation. In equation (7), n is the gas refractive index (assumed constant), N_L the Loschmidt's number ($2.54743\,10^{25}\,\mathrm{m}^{-3}$) and δ the gas depolarization constant (0.03 for terrestrial air, ignoring the λ-dependence).

As several of the parameters depend on the line-of-sight between the station ICC8 and the meteor location, thus the meteor altitude, the atmospheric correction is applied to each individual frame of a meteor event. The altitude-varying parameters are computed as follows. g and n are approximated as constants between ICC8 (the troposphere) and the meteor location (the thermosphere).

p_{top} is calculated using equation (8):

$$p = p_0 \cdot \left(1 - \frac{L \cdot h}{T_0}\right)^{\left(\frac{g \cdot M}{L \cdot R_0}\right)} \tag{8}$$

where p_0 is the SI standard pressure (101325 Pa), L the temperature lapse rate (9.76 K/km, dry air), T_0 the SI standard temperature (288.16 K), M the molar mass (0.029 kg/mol, dry air), and R_0 the universal gas constant (8.314 J/(mol·K)).

A detailed discussion of the assumptions, especially related to the atmospheric values, the improvements obtained, and potential further improvements of the correction using the atmospheric extinction correction can be found in Vicinanza et al. (2021). Figure 4 shows a spectral profile before and after the atmospheric extinction correction was applied.

This calibration step results for each frame of a meteor event in a list of wavelengths and its corresponding spectral calibrated and atmospheric corrected value are stored in a single FITS file labeled as *level-3 dataset* (see section 9 for a detailed description).

https://doi.org/10.5194/egusphere-2022-416
Preprint. Discussion started: 8 July 2022

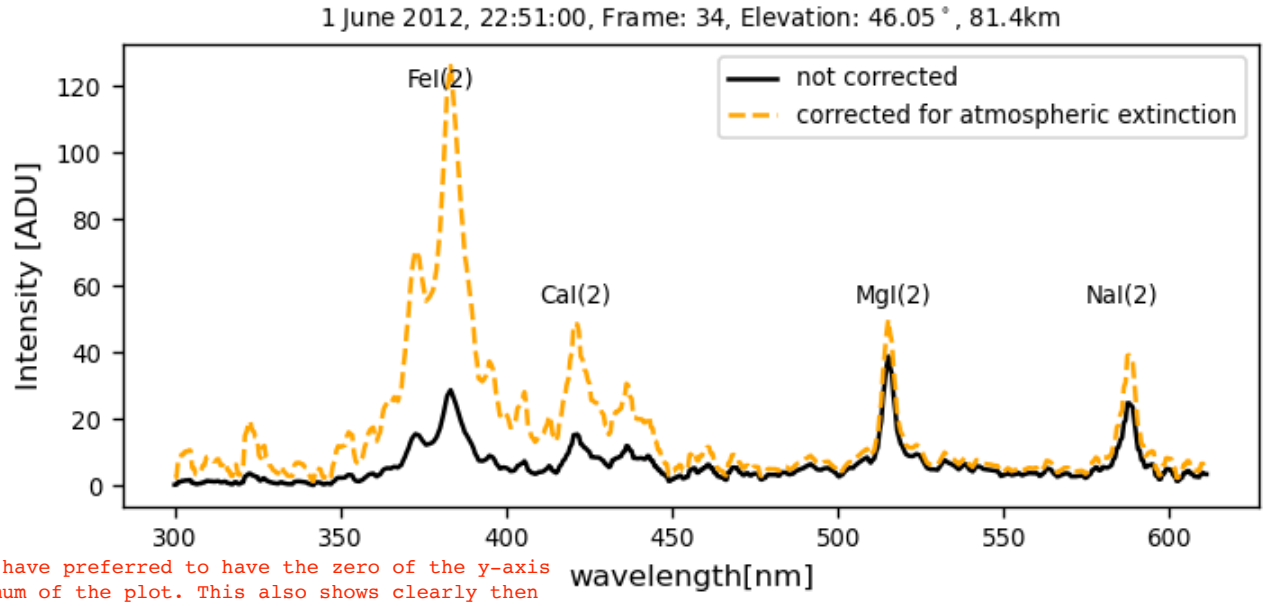

I would have preferred to have the zero of the y-axis as minimum of the plot. This also shows clearly then that the correction at shorter wavelengthes are significant.

Figure 4. Example of ICC8 spectral profile before (black) and after (red) the atmospheric extinction correction.

6 Intensity Calibration

The aim of the intensity calibration is to convert the spectral intensity, measured in CCD pixel counts often expressed as Arbitrary Digital Units (ADU), to a SI Physical units (W/m^2/nm). This allows to infer the true and absolute composition of elements in a meteoroid during the extraction of the line intensities of individual chemical elements (as will be described in Section 7). The intensity calibration is done in two steps following Jenniskens (2007): the calculation of the zero-point bias and the estimation of the coefficient of intensity calibration.

The calculation of the zero-point bias involves a photometric calibration. This is performed using the observations of A0V standard stars, simultaneously recorded in the background of meteor observations. We used Vega which has a V-band magnitude m of approximately 0. Knowing the spectral intensity of Vega observed from ICC8, expressed as the sum of ICC8 pixel brightness $\sum F$, the zero-point bias C is obtained using the relation:

$$m = C - 2.5 \log \left(\sum F, \text{ in ADU} \right) \tag{9}$$

where $\sum F$ is Vega's sum of the pixel brightness, and C is the zero-point bias we want to obtain. By applying this step to our set of CILBO observations, a value of 10.81 ± 0.1 was obtained for the zero-point bias. Theoretically, this step should be performed separately for each individual meteor event, using the stars observed in the meteor's background. However, since it was observed that the zero-point bias remains approximately constant throughout different events, a constant term was applied during our research to the calibration of all events.

https://doi.org/10.5194/egusphere-2022-416
Preprint. Discussion started: 8 July 2022

The zero-point bias is then used for the estimation of the coefficient of intensity calibration, k, according to the relation below (Jenniskens (2007)):

$$k = \frac{3.67 \times 10^{-11} \cdot 10^{-C/2.5}}{EW} \tag{10}$$

I presume equivalent width of the spectral feature.

where C is the zero-point bias and EW is the equivalent width and allows to perform a correction for the instrument aperture. Equation (10) is obtained knowing that the zero magnitude A0V standard star Vega has a flux of $3.67 \times 10^{-11} W\ \mathrm{m}^{-2}\ \mathrm{nm}^{-1}$ at 548.3 nm (V-band). On average, the coefficient k, separately calculated for each event, was around $2 \cdot 10^{-17}$ W m^{-2} nm^{-1} / ADU. Once this coefficient is obtained, the calibrated meteor spectral intensity (at each wavelength λ) is obtained from the observed meteor flux F following the relation:

$$F_{\lambda}^{cal} = k \cdot f \cdot \left(\sum F, \text{ in ADU}\right) = k_{corr} \cdot \left(\sum F, \text{ in ADU}\right) \tag{11}$$

F is the average of the flux over 10 binned pixel rows. Since the coefficient k is obtained using Vega star observations and we want to perform the intensity calibration on meteor observations, the correction factor f is needed. This accounts for the dependence of the intensity calibration coefficient k_{corr} on the exposure time of the star measurement, compared to the exposure time of the meteor measurement:

$$f = \frac{\text{exposure time star}}{\text{exposure time meteor}} \tag{12}$$

The exposure time of a Vega observation is equal to the observation time for the entire meteor event. Since we perform the intensity calibration for each meteor frame (10 binned pixel rows), the exposure time of the meteor is a ratio of the time delay between consecutive frames. Our cameras have a frame rate of 25 FPS, thus 0.04 s interval between consecutive frames (Koschny et al. (2013b)). The exposure time of the meteor in each frame can thus be obtained as:

$$\text{exposure time meteor} = \frac{0.04\,s}{\Delta y_{i,i+1}} \cdot \text{number binned pixel rows} \tag{13}$$

I presume the meteor speed always >> speed star, being sub-pixel and thus negligible.

where $\Delta y_{i,i+1}$ is the difference in y-coordinate between consecutive MetRec recordings and depends on the meteor speed.

In conclusion, the coefficient of intensity calibration k — used to convert the spectral intensity of meteors spectra from some Arbitrary Digital Units (ADU) to SI Physical units (W/m2/nm) — was considered constant for diverse observations of the same meteor event, while it changed between different meteor events. The change mostly depends on the different exposure times of different meteor events (related to the different meteor speed), the different conditions of atmospheric extinction encountered at different meteor entries, and the observational setup. In our cases, the coefficient k was in the order of $2 \cdot 10^{-17}$ W/m2/nm/ADU.

what exactly?

7 Extraction of line intensities of individual chemical elements

To determine the chemical elements and their contribution to a meteor spectral profile, a line-by-line emission simulation has to be executed for each potential chemical atom, molecule, or oxide. The atomic behaviour of each species needs to be modelled, taking into account a number of model input parameters, especially the ablation temperature and the chemical elements number

https://doi.org/10.5194/egusphere-2022-416
Preprint. Discussion started: 8 July 2022

densities. As the selection of slightly different input parameters results in a different spectral profiles that might or might not match a meteor spectral profile from the level-3 dataset, we have to solve an optimization problem. The CILBO calibration pipeline uses the Plasma Radiation Database (PARADE) line-by-line emission simulation tool (Smith, 2006). We use the Bayesian formalism to solve the optimization problem, and the PARADE tool is called from within the Bayesian method, both discussed in the following sections. This is very interesting!

7.1 The Plasma Radiation Database

The synthetic spectra are produced by ESA's PlasmA RAdiation DatabasE (PARADE) tool, originally used to simulate variation of probe entries into planetary atmosphere's (Smith, 2003; Pfeiffer et al., 2003; Liebhart et al., 2012). PARADE calculates the energy state transitions in atoms and molecules and provides the emission coefficient ϵ in radiance W/m^3/sr/m.

While the number of gaseous elements was originally restricted to the main atmospheric constituents of the atmospheres of Titan, Earth, and Mars, several new species has been added to support our spectral analysis activities for the CILBO acquired spectra. A detailed discussion is given in Loehle et al. (2021) extending the available species to include Na, K, Ti, V, Cr, Mn, Fe, Ca, Ni, Co and Li. The positional information of an emission (or absorption) line is defined by the energy gap between the electron excitation levels as defined by e.g. Herzberg (1950).

$$\Delta E = h\nu = \frac{hc}{\lambda}, \tag{14}$$

The energy levels of atoms are exclusively defined by their electron configuration and energy levels. These can be determined from the NIST database (Ralchenko and Kramida, 2020) directly. For molecules, the vibration and rotation of the nuclei are additional parameters to consider. A simple radiation model for diatomic molecules based on a Boltzmann distribution of the vibrational bands and under the assumption of thermal equilibrium, is presented in Equation 15 (Loehle et al., 2021).

$$\frac{N_J}{N} = \frac{hcA_{v,u}}{kT}(2(J-1)+1)e^{(-A_{v,u}(J-1)(J+1)100\frac{hc}{kT})} \tag{15}$$

Here h denotes the Planck constant, k the Boltzmann constant, c the vacuum speed of light, $A_{v,u}$ the Einstein coefficient for a spontaneous emission from a lower to a higher state N_J, J the rotational quantum number, and T the temperature.
In addition, we have further extended the PARADE tool by the following molecules CO, CO2, AlO, CaO, FeO, MgO, NO, and TiO.

To avoid the repetetive execution of PARADE simulations in the upcoming processing step (see Section 7.2), a database is created containing for each species the spectral response over a temperature* range from 2000K to 15000K in a 50K granularity. When building up the synthetic emission lines, FeI is processed over the full spectrum, as well as over a limited spectral width that covers explicitly the FeI (15) multiplet response, ranging between 520 to 550 nm.

In summary, the following atoms, molecules, and ions are available in our database: NaI, MgI, FeI, FeI(15), CaI, SiI, AlI, MnI, CrI, Ar, C_2, CH, CN, CO_2, FeO, CaO, AlO, MgO, O_2, OH, TiO, Na+, Mg+, Fe+, Ca+, Ar+.

* you mention here a data base on temperature. On page 12 (bottom) you mention as second parameter number density of the chemical elements. That, I presume, is not part of this database (and computed with help of the Bayesian framework)?

https://doi.org/10.5194/egusphere-2022-416
Preprint. Discussion started: 8 July 2022

7.2 Optimization of the Spectral Fitting using the Bayesian Methodology

The PARADE tool allows to compute the radiative emission of gas species by calculating the line position, its intensity and distribution, i.e. the line profile (Herzberg, 1950; Loehle et al., 2021; Rudawska et al., 2020) for a given temperature and given number density of a selected gas species.

Taking the reduced line profiles as obtained after the calibration steps (the data set level-3), a fit to the set of simulated results from the PARADE tool must be found. To solve this *inverse* problem we use the Bayesian treatment of the inference, *the Bayes' theorem*, and apply it to the meteor ablation process.

I'm a bit confused here. Is there also ablation model included in PARADE?

Having priors is of key importance in the Bayesian framework as priors express our existing knowledge about the parameter space. Parameters for which a lot of knowledge is available are named *informative priors* in the Bayesian framework. They are updated by the algorithm based on new data provided. In our case, we have three *informative priors*, all being input parameters to the PARADE simulation. First, the total number of atoms or molecules of a gaseous species directly relating to the maximum values of the simulated line profiles. We consider this number to be uniformly distributed. The temperature of a meteor ablation process is an *informative prior* and we assume a uniform distribution. Following the identification of two distinct thermal components in the meteor ablation by Jenniskens (2007), we take two distinct temperature components, T_1 and T_2, as *informative priors*.

Uninformative or *ignorance priors* are very diffuse and they do not constrain the parameters. These are used when we do not have a lot of knowledge about the parameter beforehand and are not used within the PARADE simulations. We use three *uninformative priors* in our framework.

- The PARADE tool takes into account several line broadening effects within its simulation like the Van de Waals, or natural or Stark broadening. As the errors associated with these models are not yet fully quantified, we have introduced the standard deviation of the instrumental broadening, σ, as an *uninformative prior* and consider its distribution function as uniform.

- We have reported in 5 an uncertainty in the position measurement of the meteor center that we are not able to characterize further and have therefore introduced as *uninformative prior* the uncertainty along the wavelength axis, $\Delta\lambda$, of the measured line profiles. Also for this *uninformative prior* we assume a uniform distribution.

- Moreover, the line profile itself constitutes a level of signal noise, that propagates through the algorithms (as described earlier), and is difficult to characterise. We thus introduce another *uninformative prior*, the line profile background b, assuming a Gaussian distribution.

why those 3 (only)? I could imagine more priors can be chosen. Are those considered the dominant ones? Does the computation time dramatically increase with n>3?

Finally, we need to convert the modelled synthetic spectra in irradiance (W/m3/sr/nm) into radiance (W/m2/nm). This is done by performing a solid angle conversion assuming that the meteor to have the shape of an isotropic sphere (Jenniskens (2007)). We introduce a final *uninformative prior*, the meteor's size in the direction of flight R, assuming a uniform distribution.

this is the radius of the emitting 'body' I presume (not the meteoroid size)

Table 2 lists all priors and their initial settings.

https://doi.org/10.5194/egusphere-2022-416
Preprint. Discussion started: 8 July 2022

Table 2. Overview of the parameters of our model,the choice of prior, and initial settings

parameter	description	parameter type	prior	initial setting
$\log N_X$	Logarithm of the total number of atoms or molecules of species X	*informative*	$U(-5, 35)$	
T_1 [K]	Temperature of the main spectrum	*informative*	$U(3000, 5000)$	4500
T_2 [K]	Temperature of the second spectrum	*informative*	$U(4000, 15000)$	10 000
σ [nm]	Standard deviation of the instrumental broadening	*uninformative*	$U(0, 5)$	2
$\Delta\lambda$ [nm]	Shift along the wavelength axis	*uninformative*	$N(0, 2)$	0
b	Background count rate	*uninformative*	$b^{-1/2}$	min(line profile)
R [m]	Radius of the meteor (shaped as isotropic sphere)	*uninformative*	$U(0.1, 10)$	1

The Bayesian treatment of the inference, *the Bayes' theorem* can be written as

$$P(\theta|Y) = \frac{\mathcal{L}(Y|\theta)\pi(\theta)}{\pi(Y)}. \tag{16}$$

$P(\theta|Y)$ denotes the probability of a model applied over a parameter space θ, in our case the temperature, the instrumental line broadening, the uncertainty in the wavelength, and the background count rate, given a set data samples $Y = (y_0, y_1, \dots y_N)$. y_i denotes line intensities simulated for the individual species. In literature, $P(\theta|Y)$ is typically referred to as the *posterior*. $\pi(\theta)$ are the probabilities of the parameters, the *prior*. Finally, $\pi(Y)$, typically referred to as the *evidence*, are the probabilities of the simulated line profiles.

$\mathcal{L}(Y|\theta)$, the *likelihood*, is the product of the probability of the individual data points:

$$\mathcal{L}(Y|\theta) = \prod_i^N P(y_i|\theta) \tag{17}$$

given an independent set of data points $Y = (y_0, y_1, \dots y_N)$ sampled over $X = (x_0, x_1, \dots x_N)$.

Assume we have a parameterized model $f(x|\theta)$ which models the data Y for given parameters θ and explanatory variable X, in our case the wavelength. With this model we can then calculate the probability of generating an observed data point $P(y|\theta)$, also known as the *likelihood* $\mathcal{L}(y|\theta)$. If we have an independent set of data points $Y = (y_0, y_1, \dots y_N)$ sampled over all wavelength $X = (x_0, x_1, \dots x_N)$, the total likelihood is the product of the probability of the individual data points.

https://doi.org/10.5194/egusphere-2022-416
Preprint. Discussion started: 8 July 2022

As the measured line profiles from the gaseous species are derived from CCD images, thus photon counts, the likelihood of the probability distribution line profiles over wavelength are given by a Poisson distribution.

$$\mathcal{L}(Y|\theta) = \prod_{i}^{N} \frac{f(x_i|\theta)^{y_i} \exp\left(f(x_i|\theta)\right)}{y_i!} \tag{18}$$

Instead of using the likelihood as in equation (18), it is common to work with the log-likelihood, as that reduces the product to a sum over the data points. In the Poisson case, the negative log-likelihood is given by:

$$-\ln \mathcal{L}(Y|\theta) = \sum_{i} -y_i \ln(f(x_i|\theta) + f(x_i|\theta) + \ln(y_i!) \tag{19}$$

Before we can start the Bayesian framework, an *initial guess* of the synthetic spectrum is computed, based on the values in Table 2. As we study the optically thin case (optical depth $\tau \ll 1$) and use fixed temperatures, the final, synthetic spectrum is then a linear combination of the individual emission spectra of each species as described in equation (20).

This I do not understand. How does that matter?

$$F_{\nu}^{\text{source}}(T) = \sum_{i} N_i j_{\nu,i}(T) \tag{20}$$

where F_{ν}^{source} is the flux vector of the complete source spectrum, i.e. the sum of the spectra of all species "i" at the source, N_i the number density of each species, and $j_{\nu,i}$ the temperature-dependent emission coefficient of element i. The elements' emission coefficients are retrieved from the PARADE database (introduced in Section 7.1). The flux vector F_{ν} comes from the meteor observations. The only unknowns of the equation are the number densities N_i. OK!

The estimation of the number densities of the meteor's radiating elements, is articulated in sequential three main steps: a linear regression retrieval, a nonlinear least-squares initial solution, and the final Markov Chain Monte Carlo (MCMC) parameter estimation.

For each species in our emission coefficient database (described in Section 7.1), a routine models the synthetic spectra. These are obtained through different combinations of the parameters in Table 2, left free to vary within defined boundaries (*Prior* in Table 2). A linear solution of the parameters in Table 2 is then retrieved, estimating the Moore-Penrose pseudo-inverse of the matrix having on its rows the species' synthetic spectra obtained at each combination. By applying a linear regression, considering the ICC8 observed meteor spectrum as the dependent variable, a first estimate of the number density of all the species considered is obtained.

Parada?

Using these linear estimates as first guess, a nonlinear least-squares approach is used to obtain an even more accurate estimation of the number densities' initial solution. This provides the estimate of all the unknown parameters in Table 2, whose combination generates a complete synthetic meteor which best fits the ICC8 observed meteor spectrum. The nonlinear least-squares solution for the number densities, and other parameters, is determined using the Levenberg-Marquardt algorithm. Our approach is very similar to (Benneke and Seager, 2012), where Bayesian inference is used to retrieve and constrain the composition of exoplanet atmospheres from their transit spectra. These best-fit least-squares estimates are however only an initial solution; thus do not coincide with the final best-fit solution obtained at the end of the routine, after the Markov Chain Monte Carlo (MCMC).

https://doi.org/10.5194/egusphere-2022-416
Preprint. Discussion started: 8 July 2022

The least-squares parameter estimates are used as initial guesses for the successive MCMC. Using the MCMC sampling we estimate the posterior distribution of the parameters of the spectral model. The MCMC sampler approximate the posterior distribution by generating samples with a probability that is proportional to the posterior:

$$n(\theta)d\theta \propto P(\theta|Y)d\theta, \tag{21}$$

where $n(\theta)d\theta$ is the number of samples between θ and $\theta + d\theta$. In MCMC methods we generate so-called Markov Chains which follow this distribution. A Markov Chain is a random process which obeys the Markov property that successive data point is only based on the most recent data point.

$$P(\theta_i|\theta_{i-1}\ldots\theta_{i-N}) = P(\theta_i|\theta_{i-1}). \tag{22}$$

We thus obtain not only a point estimate of the chemical composition of the meteor but an estimate of the full probability distribution, giving a constraint on the range of abundances which could describe the meteor. During the MCMC, for each meteor event 1000 iterations are run. Each iteration models a different synthetic spectrum using parameters which are sampled around the nonlinear least-squares solution via MCMC affine-invariance sampling. We use the *emcee* python package (Foreman-Mackey et al., 2013, 2019) that implements the affine-invariant ensemble sampler by Goodman and Weare (2010). The algorithm performed well under all linear transformations and is insensitive to covariances among parameters. The complete synthetic spectrum which best fits the ICC8 observed spectrum is inferred using Bayesian inference: the best-fit parameters represent those for which the posterior has highest value. Specifically, the inference returns the combination of parameters for which the modelled (synthetic) spectra best fit the observed spectra (data).

8 Spectral Calibration discussed on one meteor event

This section guides through the individual processing steps and intermediate results, based the meteor event 20131214T041302. The meteor presented was classified by METREC to belong to the Geminid shower and was observed in December 2013. The ablation was detected in 24 individual frames with a maximum apparent magnitude of -1.7.

meteor?

The level-1 FITS file contains the individual frames, as well as the total image (shown in Figure 5).

In the next processing step, the (x,y) position for each wavelength is determined frame by frame resulting in an line plot representing the meteor spectrum intensity. The profile is further spectrally calibrated and corrected for atmospheric effects resulting in a *level-2A* FITS file. The *level-2B* FITS file contains the final calibration product, after the intensity calibration is applied, in radiance ($\frac{W}{m^2 nm}$). The un-processed and calibrated profile of the brightest frame, frame 20, is shown in Figure 6.

The 1000 MCMC iterations of the ablation processes as part of the Bayesian interference algorithms are based on the priors and initial settings as given in Table 2 (see Section 7.2). In our setup - thus also applicable for this example - the initial settings used for the chemical elements are computed by a leased-square fitting algorithm and the resulting values are given in Table 3. The selection of elements for the main meteor spectrum of temperature T1 and the secondary temperature T2 (see Section 7.2) proofed stable through the processing of all meteor events. In the future, we might apply a different, larger selection of elements, i.e. when processing meteor events of a dedicated meteor shower.

Elements = chemical elements?, T1 = main, T2 = secondary?

https://doi.org/10.5194/egusphere-2022-416
Preprint. Discussion started: 8 July 2022

Figure 5. Total image (max pixel value over all frames) of event 20131214T041392 as observed by camera ICC8

Looking at the plot I wonder if the selection of chemical elements/ molecules is complete, and if not, how do the missing ones have influence in fitting model to observations?

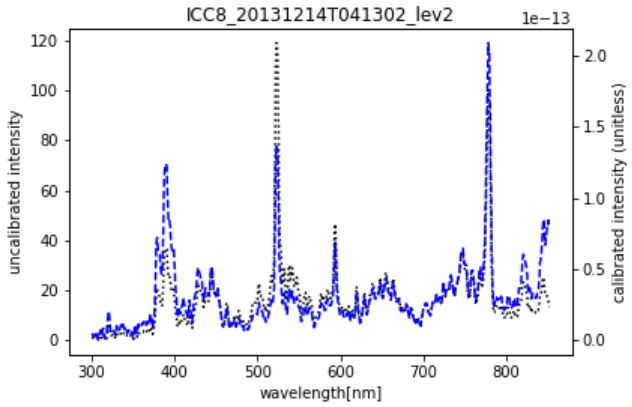

calibrated intensity unitless?

Figure 6. Un-processed (black dotted line) and calibrated (blue dashed line) profile plot of frame 20 (20131214T041392)

After the Bayesian interference algorithm and MCMC run have finished its simulations and the best fit is available, a check on the convergence of all parameters used in the simulation is needed. This is done by the visual analysis of the so called chain plot that is produced by the data pipeline for each meteor event. The chain plot visualizes the convergence of the parameters throughout the MonteCarlo iterations. Figure 7 shows the chain plot for the discussed meteor event.

what are your criteria exactly?

This validation step is currently the only manual step needed in the calibration pipeline. In case a parameter is not converging, the parameter needs to be taken out of the simulation and a rerun of the simulation is needed:

how do you do that? The node is taken out? Or the range widened?

– The two temperature regimes result in temperatures of 4000K and 9000K. The variations in the chain plots are marginal and we consider the two temperatures as an important result of our analysis.

Indeed, and they match well with Borovicka's earlier work.

https://doi.org/10.5194/egusphere-2022-416
Preprint. Discussion started: 8 July 2022

Table 3. Initial settings for elements and final results obtained. The number density is given in cm^{-3}.

could you add the wavelength of the various elements in an extra column?

element	main/secondary	number density (initial guess)	number density (result)
Fe	main	1.1×10^{7}	7.97×10^{7}
Na	main	3.9×10^{4}	3.18×10^{5}
Mg	main	1.35×10^{8}	8.14×10^{8}
Si	main	2.57×10^{10}	1.74×10^{10}
Ca	main	1×10^{-5}	1.50×10^{5}
Cr	main	3.11×10^{6}	9.99×10^{5}
Ti	main	2.3×10^{6}	1.58×10^{-4}
K	main	1×10^{-5}	9.36×10^{7}
CaO	main	1×10^{-5}	1.85×10^{-2}
FeO	main	1×10^{-5}	5.57×10^{7}
N2	main	2.16×10^{15}	2.26×10^{15}
Ca+	secondary	5.58×10^{13}	4.30×10^{-6}
Fe+	secondary	1×10^{-5}	6.97×10^{-6}
Mg+	secondary	4.95×10^{7}	1.83×10^{7}
O	secondary	3.82×10^{9}	1.38×10^{10}
N	secondary	4.13×10^{9}	7.57×10^{9}

too small to read

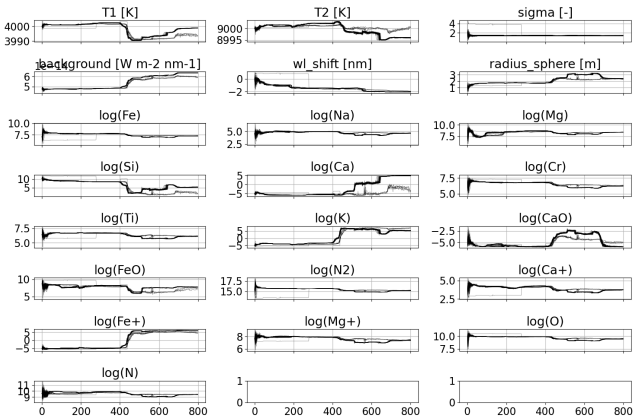

Figure 7. Un-calibrated (black dotted line) and calibrated (blue dashed line) profile plot of frame 20 (20131214T041392)

– The chemical elements Fe, Na, Mg, Si, Cr, Ti, K, CaO, FeO, N2, Ca+, Fe+, MG+, O and N converge well.

https://doi.org/10.5194/egusphere-2022-416
Preprint. Discussion started: 8 July 2022

- Only Ca shows an atypical behaviour and the log function jumps between 0 and 5. The interpretation of Ca needs to be done very carefully. why?

- The chain plot shows three other elements: background, wavelength shift, and radius_sphere. The background is a proxy for the noise level in the spectral profiles, the wavelength shift an indicator for an additional correction of the wavelength to achieve a good result (in the presented case less than 2 pixels), and radius_sphere is the radius of the meteor's luminous area. According to Jenniskens (2007), the meteor is considered as an isotropic sphere, i.e. the radiating area perpendicular to the observer has the same value across all directions of the observer, thus the luminous area equals $\pi \cdot \text{radius\_sphere}^2$.

At the end of our event analysis, the data allow the comparison of the observed spectrum to the simulated spectra obtained for the total images and the brightest frame. Figure 8 shows the obtained plots demonstrating the fitting algorithm. Most maxima in the observed spectrum are well fitted. Also the broad bands are fitted well, some overshooting is observed however between 550-650nm. The intensity of the individual frame is given on the right yaxis and is of cause less intense than in the total image. The reader shall note that the red line in Figure 8 represents the calibrated spectra in $\frac{W}{m^2 nm}$ of the brightest frame and is thus about much smaller than the corresponding black line that represents the energy of the overall meteor event (thus of all the frames).

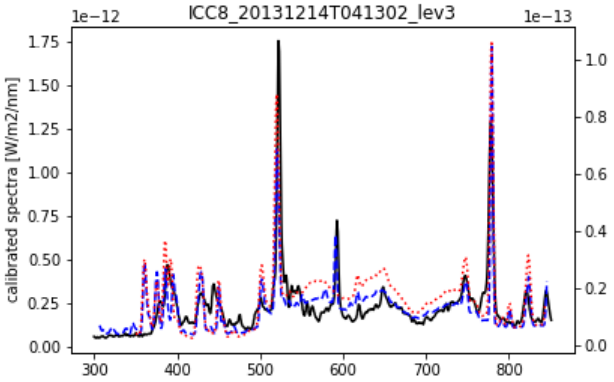

Question: is also thermal radiation included in the PARADA simulation? If not how is the continuum formed?

could you add for clarification the chemical elements?

Figure 8. Calibrated spectrum (black line), fitted spectrum based on total image (blue, dotted), and fitted spectrum of brightest frame (red, dotted) of event 20131214T041392

Table 3 contains the resulting number densities in the right column, that can be interpreted in the following way:

- From the meteoric elements, the highest number density is obtained for Si.

- The Na content is relatively small, especially in comparison to the Fe and Mg. As the Sodium is a direct indicator of the fluffiness of the meteoroid and thus it's parent body (Abe et al., 2020), this is an indication that the meteoroid might be composed of only several smaller building blocks. Our observation confirms earlier studies from e.g. Abe et al. (2020) and Vojáček et al. (2019). -> only smaller building blocks?

https://doi.org/10.5194/egusphere-2022-416
Preprint. Discussion started: 8 July 2022

refer to height

Generally, I find it difficult to derive to strong conclusions when comparing with other work, because we look only at a single event.

- Borovička (2010) and Abe et al. (2020) provided relations of Na/Mg of 0.023 and 0.067 respectively. The value we obtain for the event discussed is 0.0003, and deviates thus a lot. It has to be noted however, that our processing provide number densities and not line intensities, which might explain the difference. Could you be more conclusive here (compute the difference between number density and line itensity?)
- Borovička (2010) and Abe et al. (2020) provided relations of Fe/Mg of 0.32 and 0.3 respectively. The value we obtain is 0.09, a factor of three smaller. Borovička (2010) and Abe et al. (2020) mention however that the values of individual meteor events differ largely, by a factor of 2 for Fe/Mg and a factor of more than 10 for Na/Mg. But this still does not explain the difference to the CILBO observations. ?? I'm afraid i do not understand this
- Mg/Si and K/Si ratios of 0.046 and 0.005 respectively are in the ranges of the COSIMA instrument on-board of Rosetta (Rubin et al., 2020).
- The Na/Si ratio of 1.8×10^{-5} is however much smaller than the range given for COSIMA, that is 0.02 to 0.2 (Bardyn et al., 2017).
- The Ca/Si ratio of 8.6×10^{-6} is also much smaller than the range given for COSIMA. It must be noted that the COSIMA instrument analyzed the bulk refractory material, which might explain some of the different ratios obtained. Madiedo et al. (2013) states that Ca might not fully vaporize during the ablation which might also explain the low Ca/Si ratio.
- Cr is observed with high abundance, i.e. Cr/Na = 3.1 and Cr/Ca = 6.6. Chromium measurements were reported earlier by Russell et al. (1956) and lately by Matlovič et al. (2020). The measurements of Matlovič et al. (2019) were obtained from laboratory measurements on meteorite samples and the high Cr value was attributed to the high values of daubreelite (FeCr2S4) and enstatite (MgSi3O).
- No Ca and Fe ions are detected in the T=9000K component It is thus more surprising that the Mg ion number density is relatively large. Mg ions were reported back in Etheridge and Russell (1968). The observations discussed in Jenniskens et al. (2002) indicate that Ca, Fe, and Mg ions are a result of the hot T=10000K component, one would thus expect to find all three ionisation's back. The detailed interpretation of these observations need first to be confirmed by further detailed analysis of other events and supplemented by a better interpretation of the chemical ablation physics.

yes indeed understood

9 Available Data Sets

Table 4 summarizes the data processing levels used in the CILBO spectral calibration pipeline and in the archive.

As the processing is very intensive in respect of time and computing resources, the synthetic spectrum was computed for the total image of each event.* This is reflected in the sub-directories and in the names of the FITS structures. The data processing levels level-1 to level-3 are made publicly available via the Guest Archive Facility of ESA's Planetary Science Archive (Besse et al., 2018). All data products are stored in the FITS format (Pence et al., 2010). Level-0 represent the raw, unmodified data, level-1 data the radiometrical calibrated images, level2 data represent the spectral profiles after radiometric, camera spectral sensitivity, and altitude-dependant atmospheric extinction^{-2} corrections have been are applied. Also, the response to the intensity

* It would be very interesting to continue the work for every individual frame, the more because also altitude and velocity information exists.

https://doi.org/10.5194/egusphere-2022-416
Preprint. Discussion started: 8 July 2022

Table 4. Name, definition and format of the different levels of data within the MRG dataset.

Level	Definition	Data Format
Level-0	Raw data acquired by cameras at CILBO. No processing.	BMP (INF, LOG, SNF)
Level-1	Data after radiometric (dark current, flat-field, background subtraction) and wavelength calibration of Level 0 BMPs.	FITS
Level-2a	Data after spectral calibration of Level 1 spectra. Correction for ICC8 sensitivity and altitude-dependent atmospheric extinction.	FITS
Level-2b	Data after intensity calibration of Level 2-A spectra.	FITS
Level-3	Reduced data after MCMC Bayesian inference: chemical elements number density, ablation parameters (T, σ, b, $\Delta\lambda$) and spectra.	FITS, PNG

calibration correction is part of the level-2 data product. The level-3 data contain the derived parameters obtained from the Bayesian framework and MCMC processing: the number densities of the chemical elements, several ablation parameters, and the fitted spectra. Level-3 data are also accompanied by browse images in PNG format.

9.1 Level-1 Data

The level-1 fits files are radiometrically calibrated, thus dark current subtraction and a flatfield multiplication correction have been applied. The file names are formatted as e.g. *ICC8_20131214T041392_lev1.fits*, combining all information of one particular meteor event into a single file. The primary header provides information on the observation, the camera, and the meteor. The primary data is the total image of the event, thus each pixel represents the maximum pixel value of all frames at this position. The total image allows to obtain a quick indication on the brightness, completeness, and quality of the images available. Keyword-Value pairs in the FITS header represent information of the observation (date, time, observer, location), camera details (name, focal length, manufacturer), or the meteor event itself (brightness, meteor shower identification). Each FITS data product has 4 extensions, each being a binary table. The individual tables are structured in a similar way starting with wavelength information, information on each frame, and finally the information of the total image:

- *ICC8FRAMESINFO*, contains for each frame in the meteor event information on the frame number, the julian date, right ascension and declination in degrees (of the 0-order location obtained from ICC9), the apparent magnitude, the measured signal-to-noise ratio, a wavelength error, the number of CCD rows binned together, the distance between the camera and the meteor, the height of the meteor above ground, and the intensity calibration coefficient. In case, a parameter can not be calculated the 'nan'-value is used, which is e.g. the case when there are no double station observations are available and the *height* can not be computed.

https://doi.org/10.5194/egusphere-2022-416
Preprint. Discussion started: 8 July 2022

- the algorithm has computed based on the 0-order information available from ICC9, the location (x and y position in frame) and the corresponding wavelength for each pixel coordinate. The pixel values of these (x,y) positions are read and combined into an array, or simply profile:
- *ICC8PROFILES*, contains for each frame the derived profile based on the 0-order information
- *ICC8WAVELENGTH*, contains for each frame and for each element in the profile the corresponding wavelength. The wavelength are provided in meters.
- *ICC8SENSITIVITY*, contains the normalized instrument sensitivity curve. See Section 5 for further information.

9.2 Level-2 Data

The level-2 fits profiles are corrected for the spectral response of the camera (using the *ICC8SENSITIVITY* information) and corrected for the altitude-dependent atmospheric correction (see Section 5). The result of these corrections is stored as level–2a. The result of the intensity calibration of the level-2a profiles is stored as level-2b profiles. Whereas level-2a data is dimensionless, level-2b data are provided in $\frac{W}{m^2 nm}$

- *ICC8FRAMESINFO* is identical to level1
- *ICC8LEVEL1* is identical to ICC8PROFILES from level-1
- I*CC8LEVEL2a*, identical structure as in ICC8LEVEL1; the camera spectral calibration is applied to ICC8LEVEL1 profiles using the first array in the *ICC8SPECTRALCAL* extension as calibration curves.
- *ICC8LEVEL2b*, identical structure as in ICC8LEVEL1; the intensity (absolute) calibration is applied to *ICC8LEVEL2b* profiles
- *ICC8SPECTRALCAL*, contains the ICC8 spectral calibration curve followed by the atmospheric correction factors per wavelength for each frame.

9.3 Level-3 Data

The level-3 fits products contain the simulation results of the Bayesian method applied to the level-2 data products based on the PARADE-based database. The primary header repeats the general information on the meteor event (date, observation information, camera properties, and meteor shower information), a copy from the level-1 and level-2 data products. The two extension tables contain the gas species information for each species and considered frame:

- *TOT_IMAGE_BESTFIT*, contain for each chemical element analyzed with the Bayesian framework
  - *SPEC_TYPE* that is either *main* or *second*,
  - *NUM_DENSITY* of floating type number in scientific notation. Unit is m^{-3},

https://doi.org/10.5194/egusphere-2022-416
Preprint. Discussion started: 8 July 2022

- information on the temperature regime is given in the first two rows as two temperature regimes were analyzed,
- the Gaussian broadening, the background noise, the wavelength shift applied, and the spherical radius are independent of the elements and provided in the first row only.

- *TOT_IMAGE_SPECTRA*, contains four arrays representing the wavelength, the observed spectral profile, the synthetic spectral profile, as well as the spectral response curve used. From these arrays the spectral profile plots can be regenerated.

For validation purposes the archive contains a subdirectory named 'plots', containing for each meteor event 3 different images in PNG format.

- eventname_lev3_fit.png, a plot of the observed spectrum overlaid with the synthetic spectrum.
- eventname_lev3_elementsfit.png, contains two plots of the observed spectrum, with the synthetic spectra of each chemical element overlaid. could you include examples here?
- eventname_lev3_chain.png, contains the MCMC chain results from each chemical element used in the PARADE simulation, see Section 7.1.

10 Summary

We present an algorithm to process meteor events acquired using a camera system with a spectral grating attached to it from its raw format into quantitative chemical information. The algorithm is based on the principle that the location of a specific diffracted wavelength in 1-order can be directly derived from the knowledge of the 0-order position of the meteor. In our setup, we obtain the 0-order information from an image intensified camera, that is mounted with an offset angle to another intensified camera with a transmission grating mounted on-top. The presented algorithm includes the radiometric calibration of the images, the determination of the location of the 1-order information for each wavelength, the extraction of the meteor event spectral profile, and its spectral calibration. The spectrum derived is further corrected for atmospheric effects that take place between the observer and the location of the meteor ablation at the different heights during the event. In the next step, a Bayesian approach is used to map a simulated spectrum against the reduced spectrum obtained by our algorithm. To simulate the ablation we use the PARADE tool that was extended to allow the simulation for most meteoric and atmospheric atoms, di-atomic molecules, ions, oxides, and a few complex molecules. As pre-knowledge to the Bayesian framework we use the assumption of two main temperature regimes during the ablation, and the typical chemical elements of meteors and their respective line intensities. After running typically 1000 Markov-Chain Monte-Carlo iterations, we obtain the simulated spectrum as overall line intensities, but also obtain the line intensities of each chemical element. In a last processing step the line intensities are calibrated itself, resulting in the number densities of each chemical element.

Several hundreds of meteor events have been observed by the CILBO observatory in the past decade and we provide full access to the data in its raw and intermediate calibrated data processing levels. The data is stored using the FITS Standard, and

https://doi.org/10.5194/egusphere-2022-416
Preprint. Discussion started: 8 July 2022

an overview to the keyword-value pairs in the FITS header, as well as a description of the extended binary arrays using in the FITS extensions is provided.

A discussion of one meteor event, its processing chain, and resulting spectral information is given.

The presented algorithm works autonomous - that means without user interaction. The processing time is however large and even when using a multi-processor, multi-core system, we have not yet computed all individual frames of all meteor events. Instead, we have processed for each meteor event the information obtained from the total image as well as from the brightest frame. In the data set published, we share the data representing the total image.

All events contained in the data set has been checked for the convergence of the Bayesian parameters as result of the MCMC iterations. The list of chemical elements used in the Bayesian approach was not extensive, and in the processing so far, we only checked for the typical chemical elements also reported by other observers in the past. It is our goal to reprocess all the data and use more chemical elements that PARADE is currently able to simulate. Such a step, however, needs a very careful study of the convergence of the chemical elements - which is still a manual step and thus requiring dedicated efforts.

Acknowledgement

The work presented in this manuscript is the result of efforts over a 10-year period that was executed on a continuous, however time-limited basis. Many students supported parts of this activity and each of them contributed to this final result presented. All of these efforts have been either funded by the Science Faculty of ESA's Science Directorate or through studentships provided for by ESA. Special thanks go to Ms C. Molijn, Ms N. Bartholomae, Mr. K. Ravensberg, Mr. I. Uiarte, and Mr. J. Lightfoot. The contributions from Mr. J. Diaz del Rio, Mr. R. Landman, and Mr. L. Maraffa were highly valuable and appreciated. We would also like to thanks Prof. W. van der Wals and Prof. D. Stam for their important advice on atmospheric physics and co-lead of students.

Data availability. The meteor spectra data of the CILBO observatory are freely available at the Guest Archive Facility of ESA/ESAC. DOI:xx.xx.xx.xx

Author contributions. The activities reported in this manuscript were led and coordinated by JJZ, DVK and RR. Major contributions in the software development were done by SV and RL. SL did lead the efforts in the extension of the PARADE simulator, and LM for his advice on ablation physics* and SL on the implementation of oxides and other chemical elements into the PARADE database. HS for his continuous software support and the installation of the CILBO computing system. DS for the advice on the correction of the atmospheric effects.

* I miss a bit in the paper how this part of the work is included (or it is my lack of knowledge). Maybe you can devote 1-2 sentences to the ablation physics?

Competing interests. The contact author has declared that neither they nor their co-authors have any competing interests.

https://doi.org/10.5194/egusphere-2022-416
Preprint. Discussion started: 8 July 2022

References

Abe, S., Ogawa, T., Maeda, K., and Arai, T.: Sodium variation in Geminid meteoroids from (3200) Phaethon, Planet. Space Sci., 194, 105040, https://doi.org/10.1016/j.pss.2020.105040, 2020.

Altwegg, K., Balsiger, H., Hänni, N., Rubin, M., Schuhmann, M., Schroeder, I., Sémon, T., Wampfler, S., Berthelier, J.-J., Briois, C., Combi, M., Gombosi, T. I., Cottin, H., De Keyser, J., Dhooghe, F., Fiethe, B., and Fuselier, S. A.: Evidence of ammonium salts in comet 67P as explanation for the nitrogen depletion in cometary comae, Nature Astronomy, 4, 533–540, https://doi.org/10.1038/s41550-019-0991-9, 2020.

Appenzeller, I.: Introduction to Astronomical Spectroscopy, Cambridge University Press, 2013.

Bardyn, A., Baklouti, D., Cottin, H., Fray, N., Briois, C., Paquette, J., Stenzel, O., Engrand, C., Fischer, H., Hornung, K., Isnard, R., Langevin, Y., Lehto, H., Le Roy, L., Ligier, N., Merouane, S., Modica, P., Orthous-Daunay, F.-R., Rynö, J., Schulz, R., Silén, J., Thirkell, L., Varmuza, K., Zaprudin, B., Kissel, J., and Hilchenbach, M.: Carbon-rich dust in comet 67P/Churyumov-Gerasimenko measured by COSIMA/Rosetta, MNRAS, 469, S712–S722, https://doi.org/10.1093/mnras/stx2640, 2017.

Benneke, B. and Seager, S.: Atmospheric retrieval for super-earths: Uniquely constraining the atmospheric composition with transmission spectroscopy, Astrophysical Journal, 753, 100, https://doi.org/10.1088/0004-637X/753/2/100, 2012.

Besse, S., Vallat, C., Barthelemy, M., Coia, D., Costa, M., De Marchi, G., Fraga, D., Grotheer, E., Heather, D., Lim, T., Martinez, S., Arviset, C., Barbarisi, I., Docasal, R., Macfarlane, A., Rios, C., Saiz, J., and Vallejo, F.: ESA's Planetary Science Archive: Preserve and present reliable scientific data sets, Planet. Space Sci., 150, 131–140, https://doi.org/10.1016/j.pss.2017.07.013, 2018.

Borovicka, J.: Two components in meteor spectra, Planet. Space Sci., 42, 145–150, https://doi.org/10.1016/0032-0633(94)90025-6, 1994a.

Borovicka, J.: Line identifications in a fireball spectrum, A&AS, 103, 83–96, 1994b.

Borovička, J.: Spectroscopic Analysis of Geminid Meteors, in: Proceedings of the International Meteor Conference, 26th IMC, Bareges, France, 2007, pp. 42–51, 2010.

Borovička, J., Koten, P., Spurný, P., Boček, J., and Štork, R.: A survey of meteor spectra and orbits: evidence for three populations of Na-free meteoroids, Icarus, 174, 15–30, https://doi.org/10.1016/j.icarus.2004.09.011, 2005.

Brownlee, D.: The Stardust Mission: Analyzing Samples from the Edge of the Solar System, Annual Review of Earth and Planetary Sciences, 42, 179–205, https://doi.org/10.1146/annurev-earth-050212-124203, 2014.

Ceplecha, Z.: Determination of wave-lengths in meteor spectra by using a diffraction grating, Bulletin of the Astronomical Institutes of Czechoslovakia, 12, 246, 1961.

Ceplecha, Z.: Spectral data on terminal flare and wake of double-station meteor No. 38421 (Ondřejov, April 21, 1963), Bulletin of the Astronomical Institutes of Czechoslovakia, 22, 219, 1971.

Dubs, M. and Schlatter, P.: A practical method for the analysis of meteor spectra, WGN, Journal of the International Meteor Organization, 43, 94–101, 2015.

Etheridge, D. A. and Russell, J. A.: The Spectrum of a Meteor from the 1966 Leonid Shower, PASP, 80, 550, https://doi.org/10.1086/128676, 1968.

Foreman-Mackey, D., Hogg, D. W., Lang, D., and Goodman, J.: emcee : The MCMC Hammer , Publications of the Astronomical Society of the Pacific, 125, 306–312, https://doi.org/10.1086/670067, 2013.

https://doi.org/10.5194/egusphere-2022-416
Preprint. Discussion started: 8 July 2022

Foreman-Mackey, D., Farr, W., Sinha, M., Archibald, A., Hogg, D., Sanders, J., Zuntz, J., Williams, P., Nelson, A., de Val-Borro, M., Erhardt, T., Pashchenko, I., and Pla, O.: emcee v3: A Python ensemble sampling toolkit for affine-invariant MCMC, Journal of Open Source Software, 4, 1864, https://doi.org/10.21105/joss.01864, 2019.

Goodman, J. and Weare, J.: Ensemble samplers with affine invariance, Communications in Applied Mathematics and Computational Science, 5, 65–80, https://doi.org/10.2140/camcos.2010.5.65, 2010.

Hadamcik, E., Levasseur-Regourd, A. C., Hines, D. C., Sen, A. K., Lasue, J., and Renard, J. B.: Properties of dust particles in comets from photometric and polarimetric observations of 67P, MNRAS, 462, S507–S515, https://doi.org/10.1093/mnras/stx030, 2016.

Herzberg, G.: Molecular spectra and molecular structure. Vol.1: Spectra of diatomic molecules, 1950.

Jenniskens, P.: Quantitative meteor spectroscopy: Elemental abundances, Advances in Space Research, 39, 491–512, https://doi.org/10.1016/j.asr.2007.03.040, 2007.

Jenniskens, P., Tedesco, E., Murthy, J., Laux, C., and Price, S.: Spaceborne ultraviolet 251-384 nm spectroscopy of a meteor during the 1997 Leonid shower, MAPS, 37, 1071–1078, https://doi.org/10.1111/j.1945-5100.2002.tb00878.x, 2002.

Jenniskens, P., Gural, P., and Berdeu, A.: CAMSS: A spectroscopic survey of meteoroid elemental abundances, in: Meteoroids 2013, edited by Jopek, T. J., Rietmeijer, F. J. M., Watanabe, J., and Williams, I. P., pp. 117–124, 2014.

Koschny, D. and Diaz del Rio, J.: Meteor Orbit and Trajectory Software (MOTS) - Determining the Position of a Meteor with Respect to the Earth Using Data Collected with the Software MetRec, WGN, Journal of the International Meteor Organization, 30, 87–101, 2002.

Koschny, D., Bettonvil, F., Licandro, J., Luijt, C. v. d., Mc Auliffe, J., Smit, H., Svedhem, H., de Wit, F., Witasse, O., and Zender, J.: A double-station meteor camera set-up in the Canary Islands - CILBO, Geoscientific Instrumentation, Methods and Data Systems, 2, 339–348, https://doi.org/10.5194/gi-2-339-2013, 2013a.

Koschny, D., Bettonvil, F., Licandro, J., Luijt, C. v. d., Mc Auliffe, J., Smit, H., Svedhem, H., de Wit, F., Witasse, O., and Zender, J.: A double-station meteor camera set-up in the Canary Islands - CILBO, Geoscientific Instrumentation, Methods and Data Systems, 2, 339–348, https://doi.org/10.5194/gi-2-339-2013, 2013b.

Koschny, D., Mc Auliffe, J., Drolshagen, E., Bettonvil, F., Licandro, J., van der Luijt, C., Ott, T., Smit, H., Svedhem, H., Witasse, O., and Zender, J.: CILBO - Lessons learned from a double-station meteor camera setup in the Canary Islands, in: Proceedings of the International Meteor Conference, Giron, France, 18-21 September 2014, edited by Rault, J. L. and Roggemans, P., pp. 10–15, 2014.

Koschny, D., Albin, T., Drolshagen, E., Drolshagen, G., Drolshagen, S., Koschny, J., Kretschmer, J., van der Luijt, C., Molijn, C., Ott, T., Poppe, B., Smit, H., Svedhem, H., Toni, A., de Wit, F., and Zender, J.: Current activities at the ESA/ESTEC Meteor Research Group, in: International Meteor Conference Mistelbach, Austria, p. 204, 2015a.

Koschny, D., Albin, T., Drolshagen, E., Drolshagen, G., Drolshagen, S., Koschny, J., Kretschmer, J., van der Luijt, C., Molijn, C., Ott, T., Poppe, B., Smit, H., Svedhem, H., Toni, A., de Wit, F., and Zender, J.: Current activities at the ESA/ESTEC Meteor Research Group, in: International Meteor Conference Mistelbach, Austria, p. 204, 2015b.

Koschny, D., Drolshagen, E., Drolshagen, S., Kretschmer, J., Ott, T., Drolshagen, G., and Poppe, B.: Flux densities of meteoroids derived from optical double-station observations, Planet. Space Sci., 143, 230–237, https://doi.org/10.1016/j.pss.2016.12.007, 2017.

Koschny, D., Soja, R. H., Engrand, C., Flynn, G. J., Lasue, J., Levasseur-Regourd, A.-C., Malaspina, D., Nakamura, T., Poppe, A. R., Sterken, V. J., and Trigo-Rodríguez, J. M.: Interplanetary Dust, Meteoroids, Meteors and Meteorites, Space Sci. Rev., 215, 34, https://doi.org/10.1007/s11214-019-0597-7, 2019.

https://doi.org/10.5194/egusphere-2022-416
Preprint. Discussion started: 8 July 2022

Koschny, D. V., McAuliffe, J., Bettonvil, F. C. M., Gritsevich, M., van der Luijt, C., Ocaña, F., Smit, H., Svedhem, H., and Zender, J. J.: What happened at ESA's Meteor Research Group in 2010/11?, in: Proceedings of the International Meteor Conference, 30th IMC, Sibiu, Romania, 2011, pp. 57–60, 2012.

Lang, D., Hogg, D. W., Mierle, K., Blanton, M., and Roweis, S.: Astrometry.net: Blind Astrometric Calibration of Arbitrary Astronomical Images, AJ, 139, 1782–1800, https://doi.org/10.1088/0004-6256/139/5/1782, 2010.

Levasseur-Regourd, A.-C., Agarwal, J., Cottin, H., Engrand, C., Flynn, G., Fulle, M., Gombosi, T., Langevin, Y., Lasue, J., Mannel, T., Merouane, S., Poch, O., Thomas, N., and Westphal, A.: Cometary Dust, Space Sci. Rev., 214, 64, https://doi.org/10.1007/s11214-018-0496-3, 2018.

Loehle, S., Eberhart, M., Zander, F., Meindl, A., Rudawska, R., Koschny, D., Zender, J., Dantowitz, R., and Jenniskens, P.: Extension of the plasma radiation database PARADE for the analysis of meteor spectra, MAPS, 56, 352–361, https://doi.org/10.1111/maps.13622, 2021.

Madiedo, J. M.: Spectroscopy of a κ-Cygnid fireball afterglow, Planet. Space Sci., 118, 90–94, https://doi.org/10.1016/j.pss.2015.03.015, 2015.

Madiedo, J. M., Trigo-Rodríguez, J. M., Castro-Tirado, A. J., Ortiz, J. L., and Cabrera-Caño, J.: The Geminid meteoroid stream as a potential meteorite dropper: a case study, MNRAS, 436, 2818–2823, https://doi.org/10.1093/mnras/stt1777, 2013.

Matlovič, P., Tóth, J., Rudawska, R., Kornoš, L., and Pisarčíková, A.: Spectral and orbital survey of medium-sized meteoroids, A&A, 629, A71, https://doi.org/10.1051/0004-6361/201936093, 2019.

Matlovič, P., Tóth, J., Kornoš, L., and Loehle, S.: On the sodium enhancement in spectra of slow meteors and the origin of Na-rich meteoroids, Icarus, 347, 113817, https://doi.org/10.1016/j.icarus.2020.113817, 2020.

Pence, W. D., Chiappetti, L., Page, C. G., Shaw, R. A., and Stobie, E.: Definition of the Flexible Image Transport System (FITS), version 3.0, A&A, 524, A42, https://doi.org/10.1051/0004-6361/201015362, 2010.

Ralchenko, Y. and Kramida, A.: Development of NIST Atomic Databases and Online Tools, Atoms, 8, 56, https://doi.org/10.3390/atoms8030056, 2020.

Rivilla, V. M., Drozdovskaya, M. N., Altwegg, K., Caselli, P., Beltrán, M. T., Fontani, F., van der Tak, F. F. S., Cesaroni, R., Vasyunin, A., Rubin, M., Lique, F., Marinakis, S., Testi, L., Rosina Team, Balsiger, H., Berthelier, J. J., de Keyser, J., Fiethe, B., Fuselier, S. A., Gasc, S., Gombosi, T. I., Sémon, T., and Tzou, C. Y.: ALMA and ROSINA detections of phosphorus-bearing molecules: the interstellar thread between star-forming regions and comets, MNRAS, 492, 1180–1198, https://doi.org/10.1093/mnras/stz3336, 2020.

Rubin, M., Engrand, C., Snodgrass, C., Weissman, P., Altwegg, K., Busemann, H., Morbidelli, A., and Mumma, M.: On the Origin and Evolution of the Material in 67P/Churyumov-Gerasimenko, Space Sci. Rev., 216, 102, https://doi.org/10.1007/s11214-020-00718-2, 2020.

Rudawska, R., Zender, J., Jenniskens, P., Vaubaillon, J., Koten, P., Margonis, A., Tóth, J., McAuliffe, J., and Koschny, D.: Spectroscopic Observations of the 2011 Draconids Meteor Shower, Earth Moon and Planets, 112, 45–57, https://doi.org/10.1007/s11038-014-9436-8, 2014.

Rudawska, R., Zender, J., Koschny, D., Smit, H., Löhle, S., Zander, F., Eberhart, M., Meindl, A., and Latorre, I. U.: A spectroscopy pipeline for the Canary island long baseline observatory meteor detection system, Planet. Space Sci., 180, 104773, https://doi.org/10.1016/j.pss.2019.104773, 2020.

Russell, J. A., Sadoski, Michael J., J., Sadoski, D. C., and Wetzel, G. F.: The Spectrum of a Geminid Meteor, PASP, 68, 64, https://doi.org/10.1086/126881, 1956.

Smith, A. J.: Plasma radiation database parade v2.2, Technical Report TR 28/96 Issue 3., Tech. rep., Emsworth, UK: Fluid Gravity Engineering Ltd., 2006.

https://doi.org/10.5194/egusphere-2022-416
Preprint. Discussion started: 8 July 2022

Snodgrass, C., A'Hearn, M. F., Aceituno, F., Afanasiev, V., Bagnulo, S., Bauer, J., Bergond, G., Besse, S., Biver, N., Bodewits, D., Boehnhardt, H., Bonev, B. P., Borisov, G., Carry, B., Casanova, V., Cochran, A., Conn, B. C., Davidsson, B., Davies, J. K., de León, J., de Mooij, E., de Val-Borro, M., Delacruz, M., DiSanti, M. A., Drew, J. E., Duffard, R., Edberg, N. J. T., Faggi, S., Feaga, L., Fitzsimmons, A., Fujiwara, H., Gibb, E. L., Gillon, M., Green, S. F., Guijarro, A., Guilbert-Lepoutre, A., Gutiérrez, P. J., Hadamcik, E., Hainaut, O., Haque, S., Hedrosa, R., Hines, D., Hopp, U., Hoyo, F., Hutsemékers, D., Hyland, M., Ivanova, O., Jehin, E., Jones, G. H., Keane, J. V., Kelley, M. S. P., Kiselev, N., Kleyna, J., Kluge, M., Knight, M. M., Kokotanekova, R., Koschny, D., Kramer, E. A., López-Moreno, J. J., Lacerda, P., Lara, L. M., Lasue, J., Lehto, H. J., Levasseur-Regourd, A. C., Licandro, J., Lin, Z. Y., Lister, T., Lowry, S. C., Mainzer, A., Manfroid, J., Marchant, J., McKay, A. J., McNeill, A., Meech, K. J., Micheli, M., Mohammed, I., Monguió, M., Moreno, F., Muñoz, O., Mumma, M. J., Nikolov, P., Opitom, C., Ortiz, J. L., Paganini, L., Pajuelo, M., Pozuelos, F. J., Protopapa, S., Pursimo, T., Rajkumar, B., Ramanjooloo, Y., Ramos, E., Ries, C., Riffeser, A., Rosenbush, V., Rousselot, P., Ryan, E. L., Santos-Sanz, P., Schleicher, D. G., Schmidt, M., Schulz, R., Sen, A. K., Somero, A., Sota, A., Stinson, A., Sunshine, J. M., Thompson, A., Tozzi, G. P., Tubiana, C., Villanueva, G. L., Wang, X., Wooden, D. H., Yagi, M., Yang, B., Zaprudin, B., and Zegmott, T. J.: The 67P/Churyumov-Gerasimenko observation campaign in support of the Rosetta mission, Philosophical Transactions of the Royal Society of London Series A, 375, 20160249, https://doi.org/10.1098/rsta.2016.0249, 2017.

Vaubaillon, J., Koten, P., Margonis, A., Toth, J., Rudawska, R., Gritsevich, M., Zender, J., McAuliffe, J., Pautet, P.-D., Jenniskens, P., Koschny, D., Colas, F., Bouley, S., Maquet, L., Leroy, A., Lecacheux, J., Borovicka, J., Watanabe, J., and Oberst, J.: The 2011 Draconids: The First European Airborne Meteor Observation Campaign, Earth Moon and Planets, 114, 137–157, https://doi.org/10.1007/s11038-014-9455-5, 2015.

Vicinanza, S., Koschny, D., Rudawska, R., Stam, D., van der Wal, W., and Zender, J.: Spectral Calibration of Meteors: An Elevation-Dependent Atmospheric Correction, WGN, Journal of the International Meteor Organization, 49, 201–210, 2021.

Vojáček, V., Borovička, J., Koten, P., Spurný, P., and Štork, R.: Properties of small meteoroids studied by meteor video observations, A&A, 621, A68, https://doi.org/10.1051/0004-6361/201833289, 2019.

Ward, W.: Video meteor spectroscopic and orbital observations, 2015 April to 2016 April, Journal of the British Astronomical Association, 127, 217–222, 2017.

Zender, J.: Line identifications in a fireball spectrum, A&AS, 103, 83–96, 1994.

Zender, J., Koschny, D., and Ravensberg, K.: Calibration of spectral video observations in the visual: theoretical overview of the ViDAS calibration pipeline, in: Proceedings of the International Meteor Conference, Poznan, Poland, 22-25 August 2013, edited by Gyssens, M., Roggemans, P., and Zoladek, P., pp. 126–129, 2014.

Zender, J. J., Witasse, O., Koschny, D. V., Trautner, R., Knöfel, A., Diaz del Rio, J., and Quicke, G.: First results of spectroscopic measurements during the ESA Leonid campaign 2001, in: Asteroids, Comets, and Meteors: ACM 2002, edited by Warmbein, B., vol. 500 of *ESA Special Publication*, pp. 121–125, 2002.